Article

Multi-Omics Analysis Reveals Signaling-Metabolic Reprogramming Crosstalk during Celastrol-Mediated Inflammatory Response

Guangshan Xie [1,2], Lin Zhu [2,*], Xin Diao [2], Xiuli Su [3], Li Zhong [2], and Zongwei Cai [2,3,*]

[1] POPs Lab, Shenzhen Center for Disease Control and Prevention, Shenzhen 518055, China
[2] State Key Laboratory of Environmental and Biological Analysis, Department of Chemistry, Hong Kong Baptist University, Hong Kong SAR, China
[3] Eastern Institute of Technology, Ningbo 315200, China
* Correspondence: zhu_lin@hkbu.edu.hk (L.Z.); zwcai@hkbu.edu.hk (Z.C.)

Abstract: Celastrol (CEL), a bioactive compound derived from *Tripterygium wilfordii*, exerts potent anti-inflammatory and metabolic-regulating properties, though its underlying mechanisms remain incompletely elucidated. Herein, we combined phosphoproteomics, targeted lipidomics, and metabolomics to delineate how CEL reprograms macrophage metabolism to resolve inflammation. Temporal phosphoproteomic analysis in LPS-stimulated macrophages revealed that CEL dynamically suppressed phosphorylation events across inflammatory pathways, with the PI3K/AKT/mTOR axis emerging as a central regulated pathway. We successfully quantified 18 PIP2 and 14 PIP3 species by shotgun lipidomics and found that CEL significantly reduced PIP3/PIP2 ratios, inhibiting PI3K activity and attenuating mTOR-dependent phosphorylation of downstream effectors. We further found that the suppression of PI3K disrupted HIF-1α stabilization and nuclear translocation, reversing LPS-driven metabolic shifts: CEL dampened glycolysis while restoring oxidative phosphorylation (OXPHOS) and rectifying TCA cycle fragmentation, as evidenced by reduced succinate/α-ketoglutarate ratios. CEL skewed macrophages toward an anti-inflammatory M2 phenotype, marked by downregulated CD86 and upregulated CD163. Overall, we unveil HIF-1α as a critical mediator of CEL's anti-inflammatory effect, bridging phosphoprotein signaling rewiring to metabolic reprogramming. This mechanistic insight positions CEL as a therapeutic candidate for inflammatory diseases via metabolic modulation.

Keywords: multi-omics analysis; celastrol; signaling pathway; metabolic reprogramming; inflammatory response

1. Introduction

Celastrol (CEL), a quinone methide triterpene, has been identified as one of the most pharmacologically active components extracted from a traditional Chinese medicinal plant named *Tripterygium wilfordii* (also known as thunder god vine). Extensive studies have confirmed the anti-inflammatory and immunosuppressive properties of CEL, allowing it to be effectively used in the treatment of inflammatory and metabolic diseases, such as rheumatoid arthritis and obesity [1–3]. In particular, CEL showed rapid anti-inflammation and immunosuppression effects within a few hours of treatment in various immune cell models. For instance, the secretion of cytokines IL-1β and TNF in THP-1 cells was significantly inhibited by CEL following 1 h of incubation [4]. Luo et al. [5] also found that pre-treatment of CEL for 1 h suppressed LPS-induced expression of proinflammatory macrophage biomarkers, including IL-6, IL-1β, iNOS, TNF-α, CCL2, and CXCL-10 in murine macrophage RAW264.7 cells. However, the underlying mechanism of these CEL's pharmacological effects is not fully understood.

Macrophages, as an important component of the innate immune system, play a crucial role in the inflammatory response and the progression of inflammatory diseases [6]. In response to various environmental conditions, macrophages differentiate into different subtypes with distinct functions, including classically activated or inflammatory M1-like macrophages and alternatively activated or anti-inflammatory M2-like macrophages [7]. During the immune response, macrophages usually switch between different phenotypic states to guarantee their function in innate immunity, yet disruption of this process is closely associated with many inflammatory diseases [8]. The shift of macrophages to different functional states is coupled with and dependent

on metabolic reprogramming [9]. Metabolic reprogramming, as a hallmark of the inflammatory response in macrophages, typically undergoes a transition from oxidative phosphorylation (OXPHOS) to glycolysis or other alterations in metabolic pathways. Thus, figuring out the role of CEL in macrophage metabolic reprogramming may facilitate clarification of the mechanism underlying the anti-inflammatory and immunosuppressive effects of CEL.

Macrophages integrate various signaling cascades to generate proper responses and thus respond effectively to a variety of internal and external stimuli. These signaling pathways are closely coupled to core metabolic pathways and consequently exert significant regulatory effects on both the instant function and the long-term fate of macrophages [10,11]. Particularly, several pathways have been proposed to drive metabolic remodeling in macrophages [12]. Signaling pathways constitute a series of protein phosphorylation and dephosphorylation events which provide specific and fine-grained control of signal transduction by multi-regulatory feedback loops. Mass spectrometry (MS)-based phosphoproteomics has emerged as a major platform for unbiased, quantifiable identification of phosphoproteins and phosphosites on a global scale, making it a powerful tool for capturing phosphorylation events involved in signaling pathways [13]. So far, there is limited comprehensive analysis regarding phosphoproteomics, lipidomics, and metabolomics to map signaling-metabolic crosstalk involved in CEL-mediated inflammatory response.

To resolve these obstacles, MS-based phosphoproteomics was employed to unravel dynamic changes of CEL-mediated signal networks and identify key signal modules of metabolic remodeling in lipopolysaccharide (LPS)-stimulated rat macrophages. Moreover, targeted lipidomics quantified dozens of PIP2 and PIP3 species and revealed the reduced PIP3/PIP2 ratios by CEL, which confirmed the central role of PI3K/AKT/mTOR signaling pathway in CEL-mediated inflammatory response. Its downstream regulator, HIF-1α, was further identified as a key regulator of CEL-mediated macrophage metabolic reprogramming by suppressing glycolysis and improving oxidative phosphorylation (OXPHOS) in LPS-activated macrophages. Also, the targeted metabolomics revealed that CEL inhibited glycolytic metabolites and blocked tricarboxylic acid (TCA) cycle fragmentation, metabolically suppressing inflammatory responses. Therefore, our multi-omics analysis facilitated a comprehensive insight into the regulatory mechanisms of CEL in macrophage metabolic reorganization and suggested that HIF-1α would be a viable target for the treatment of inflammation-related diseases.

2. Materials and Methods

2.1. Cell Culture

The rat alveolar macrophage cell line (NR8383) was purchased from the American Type Culture Collection (ATCC, Manassas, VA, USA). Macrophages were thawed and cultivated with Ham's F12K medium (Gibco, Waltham, MA, USA) supplemented with 15% fetal bovine serum, 0.1% Penicillin, and Streptomycin (Thermo, Waltham, MA, USA). Cells were kept in a humid incubator set at 37 °C with 5% CO_2.

2.2. Sample Separation and Enrichment for Phosphoproteome

The preparation of phosphorylated proteomes followed the methodology used in our previous study [14]. Cells were pretreated with CEL (CAS:34157-83-0, Sigma, Darmstadt, Germany) or an equal volume of dimethyl sulfoxide (DMSO, Sigma, Darmstadt, Germany) at a final concentration of 1 μM for 1 h and then stimulated with 100 ng/mL LPS (Sigma, Darmstadt, Germany) for 1 h. After treatment, cells were washed with ice-cold Tris-buffered saline (TBS) and incubated in lysis buffer (8 M Urea, 50 mM triethylammonium bicarbonate (TEAB), 4% SDS, 5 mM EDTA, 50 mM β-glycerophosphate (Sigma, Darmstadt, Germany), 5 mM sodium orthovanadate (Sigma, Darmstadt, Germany), protease and phosphatase inhibitor cocktail (Roche, Basel, Switzerland), PH 8) at room temperature (RT) for 5 min. Lysate was collected and precipitated using five times the volume of pre-chilled acetone at −20 °C overnight. Protein pellets were dissolved in 50 mM TEAB supplemented with protease and phosphatase inhibitor mixture (Roche, Basel, Switzerland). The protein concentration was determined by BCA assay (Thermo, Waltham, MA, USA). Proteins (~3 mg) from each sample were cleaned and digested by using the FASP method previously described [15]. Briefly, protein samples were added into YM-30 microcon filter units (Millipore, Darmstadt, Germany) and centrifuged at 12,000× *g* at 12 °C for 5 min. Samples were then reduced using 5 mM Dithiothreitol (DTT, Sigma, Darmstadt, Germany) at 56 °C for 1 h, followed by alkylation with 15 mM iodoacetamide (IAA, Sigma, Darmstadt, Germany) in the dark at RT for 40 min. Four buffer exchange steps were performed with 50 mM TEAB to remove excess IAA. Proteins were digested at 37 °C overnight by sequentially adding Endoproteinase Lys-C (Thermo, Waltham, MA, USA) and Trypsin (Sigma, Darmstadt, Germany) with a ratio of 1:200 and 1:50 (*w*/*w*), respectively. The digested peptides were desalted by Solid-Phase Extraction (SPE) columns (Waters, Milford, MA, USA) for further phosphopeptide enrichment.

The enrichment of phosphopeptides was performed using titanium dioxide (TiO$_2$, GL Sciences, Tokyo, Japan). TiO$_2$ beads (12 mg beads/1 mg protein, GL Sciences, Tokyo, Japan) were conditioned with 800 µL 0.1% TFA and 80% acetonitrile (solution A) and equilibrated with phosphopeptide binding buffer containing 20% lactic acid in solution A (solution B). Desalted peptides were resuspended in 800 µL solution B and mixed with conditioned TiO$_2$ beads. The mixture was then incubated with gentle rotation for 1.5 h at RT. After centrifuging at 3000× *g* for 1 min, TiO$_2$ beads were sequentially washed twice with solution B and solution A. Phosphopeptides were eluted with 60 µL PBS, 5% ammonium hydroxide (Sigma, Darmstadt, Germany), and 5% pyrrolidine (Sigma, Darmstadt, Germany) in sequence. After acidification with 20% formic acid, eluted samples were dried by a vacuum concentrator (N-Biotek, Bucheon, South Korea).

2.3. Stable Isotope Dimethyl Labeling for Phosphopeptides

On-stage tip labeling was performed for phosphopeptide labeling in this study. Briefly, desalted phosphopeptides were reconstituted in 60 µL of 1% TFA and loaded into conditioned Stagetips by 60 µL of 0.1% TFA in 80% ACN and 0.1% TFA. Afterwards, Stagetips were washed with 0.1% TFA twice and then flushed ten times with 60 µL of the 'light' (20% CH$_2$O, 3 M NaBH$_3$CN in 100 mM Na$_2$H$_2$PO$_4$) and 'heavy' (20% ^{13}CH$_2$O, 3 M NaBD$_3$CN in 100 mM Na$_2$H$_2$PO$_4$) labeling reagent with the exact mass of 28.0313 Da and 36.0757 Da, respectively, resulting in a mass difference of 8.0444 mDa between labeled peptides. Labeled samples were washed with 0.1% TFA and eluted with 60% ACN containing 0.1% TFA. The differentially labeled samples were mixed and dried by vacuum centrifugation for further LC-MS/MS analysis.

2.4. Nano LC-MS/MS Analysis for Phosphopeptides

Labeled phosphopeptide samples were analyzed by an Orbitrap Fusion Tribrid mass spectrometer (Thermo, Waltham, MA, USA) in positive mode coupled to an Ultimate 3000 nano-LC system (Thermo, Waltham, MA, USA). Samples were loaded on a self-packed C18 analytical reverse phase column (75 µm × 12 cm, 3 µm, 200 Å) and separated with a gradient of 2–50% mobile-phase solvent B (ACN in 0.1% FA) over 120 min at a flow rate of 200 nl/min at 55 °C. Separated peptides were analyzed by the XCalibur-controlled Orbitrap Fusion Tribrid mass spectrometer in data-dependent acquisition (DDA) mode. The MS1 spectra were acquired from 350 to 1550 *m/z* at an Orbitrap of 60,000 resolution. Top abundant MS1 peaks were fragmented for high-energy collision-induced dissociation (HCD) with 35% collision energy. The resulting MS2 spectra at a charge state of 2–4 were acquired at 150,000 resolution with 3 s cycle time. The MS1 and MS2 scans were performed with an automatic gain control (AGC) of 4.0×10^5 and 5.0×10^4 and a maximal injection time of 50 ms and 45 ms, respectively.

2.5. Phosphoproteomic MS/MS Data Analysis

All raw data files were searched with the Maxquant software (Version 1.6.5.0) against the Rat UniProt database (9924 entries). Data search was set as default, and DimrthLys 0, DimethylNter 0, and DimthLys 8, DimethylNter 8 were selected for the quantitation group. Two missed cleavages were allowed for trypsin and lysine C digestion. Oxidation(M), Acetyl (*N*-term), and phosphorylation (Ser, Thr, and Tyr) were set as variable modifications and carbamidomethyl (C) as the fixed modification. The tolerance of peptide match and reporter mass was set at 20 ppm and 0.01 Da. A minimum of two ratios was required to quantify a phosphosite with an FDR of 1%. Quantification result in different experimental groups was obtained from the normalized ratios of the intensity of reporter ions. Phosphosites with adjusted $p < 0.05$ (Student's *t*-test) and fold of change > 50% were chosen as significantly up-regulated and down-regulated.

Gene Ontology (GO) annotations and KEGG pathway enrichment analysis were conducted using the online platform David (https://davidbioinformatics.nih.gov (accessed on 5 July 2024)). The significantly changed proteins and PTM-proteins were classified, and only GO terms and biological pathways with *p* values < 0.05 were considered as statistically significantly enriched.

2.6. PRM-Targeted Analysis of Phosphoproteome

Cell samples were collected from two groups (CEL and control) after stimulating with LPS for 0, 1, 2, and 3 h. Phosphopeptide samples without labeling for MS/MS analysis were prepared as described above. The DDA data of peptide samples were obtained by Orbitrap Fusion as in dimethyl labeling experiments and then searched by Proteome Discoverer (PD) 1.4 (Thermo, Waltham, MA, USA). Search results were imported into Skyline-Daily (Version 3.7) to generate a PRM detection list including precursor *m/z*, charge, and retention time window. A high ion signal in the spectra library from GAPDH was used as a normalization standard to reduce experimental errors.

The PRM-based MS/MS analysis was performed in position ion mode, and the parameters were as follows: 60,000 resolution with a *m/z* scan range of 350 to 1000 for MS1 scan. The maximum IT was 50 ms with 4.0×10^5 of AGC. The following tMS2 data were collected at a resolution of 30,000 with an isolation window of 2 *m/z*. An HCD collision cell with 35% collision energy was used for fragmentation. All PRM acquisition data from three replicates for each sample were imported to Skyline again for further quantification. Peptide settings for Skyline were the same as parameters of Proteome Discoverer Software (Thermo, Waltham, MA, USA) search, and the transition settings were as follows: charges for precursor and ion were 2–4 and 1,2, respectively. The tolerance was 0.05 *m/z,* and top 6 strongly intense ions were selected. The intensity of product ions was exported and normalized with the intensity of internal reference protein to calculate the relative abundance.

2.7. Western Blotting

Cells were lysed in RIPA buffer (Beyotime, Shanghai, China) containing protease inhibitors (Roche, Basel, Switzerland). Specifically, nuclear extracts were prepared using Nuclear Extraction Kit (#ab219177, Abcam, Cambridge, UK) for detecting nuclear HIF-1A and phosphorylated HIF-1A expression. Lysate was quantified using a BCA Protein Assay Kit (Thermo, Waltham, MA, USA) followed by boiling in Laemmli sample buffer for 5 min at 95 °C. Samples were separated on 10% SDS-PAGE gels and transferred to polyvinylidene difluoride (PVDF) membranes (Millipore, Darmstadt, Germany). The membranes were blocked with Membrane Blocking Solution (Thermo, Waltham, MA, USA) for 2 h at RT and then incubated with indicated primary antibodies at 4 °C overnight. After washing three times with Tris-buffered saline-Tween (TBST), the membranes were incubated with a 1:5000 dilution of appropriate horseradish peroxidase (HRP)-conjugated goat anti-mouse and anti-rabbit IgG secondary antibody (#31431 & #65-6120, Invitrogen, Carlsbad, CA, USA, 1:2000) for 2 h at RT and washed three more times with TBST. The immunoblots were incubated in ECL western blotting chemiluminescent substrates (Thermo, Waltham, MA, USA) for 1 min and visualized using the LI-COR Imaging System (LI-COR, Lincoln, NE, USA). Primary antibodies used in this study: mouse anti-GAPDH (#AC002, ABclonal, Wuhan, China, 1:4000), rabbit anti-RPS6 (#A6058, ABclonal, Wuhan, China, 1:1000), rabbit anti-phospho-RPS6-S235/236 (#AP0538, ABclonal, Wuhan, China, 1:1000), rabbit anti-phospho-EIF4BP1-T70 (#AP0031, ABclonal, Wuhan, China, 1:1000), rabbit anti-eIF4BP1 (#A1248, ABclonal, Wuhan, China, 1:1000), rabbit anti-AKT1S1 (#A6238, ABclonal, Wuhan, China, 1:1000), rabbit anti-phospho-AKT1S1-T246 (#AP0793, ABclonal, Wuhan, China, 1:500), anti-phospho-AKT1S1-S183 (PA5-78600, Invitrogen, Waltham, MA, USA, 1:1000), rabbit anti-CD163 (#ab182422, Abcam, Cambridge, UK, 1:1000), rabbit anti-CD86 (#ab220188, Abcam, Cambridge, UK, 1:200), mouse anti-AKT (# 9272, Cell Signaling, Danvers, MA, USA, 1:1000), rabbit anti-phosphor-AKT-S473 (#9271, Cell Signaling, Danvers, USA, 1:1000), rabbit anti-HIF-1α (#PA3-16521, Invitrogen, Waltham, MA, USA, 1:1000), rabbit anti-phospho-HIF1A-S641/S643(#AF0062, Affinity Biosciences, Cincinnati, OH, USA, 1:500).

2.8. Quantification of Derivatized Phosphoinositide Species

Cells (~2×10^7) were collected and lysed in 1 mL of ice-cold MeOH/H$_2$O/CHCl$_3$ (6:4:3, *v/v/v*) for 10 min at RT. Pellets were resuspended in 1 mL of MTBE/MeOH/2NHCl (200:60:13, *v/v/v*) and vortexed for 10 min. 250 μL of 1 M HCl was added and subsequently vortexed for 2 min. Phase separation was obtained by centrifugation at 6500 g for 2 min; the upper organic phase was collected into new tubes and dried in a vacuum concentrator. Dried samples were resuspended in 100 μL of methanol: dichloromethane: TMS-diazomethane (4:5:1) containing 20 ng/μL of internal standards (di8:0 PI (4,5) P$_2$ and 17:0, 20:4 PI (3,4,5) P$_3$) by vortexing for 1 h at RT. The reaction was ended by adding 1 μL of glacial acetic acid. Samples were dried again by vacuum concentration for the following MS analysis. The dried, derivatized samples were dissolved in 200 μL of 2000-fold diluted saturated LiCl methanol solution and analyzed by a TSQ Quantiva^{TM} triple-quadrupole mass spectrometer (Thermo, Waltham, MA, USA). A heated electrospray ionization (HESI) source with an ionization voltage of 3.5 kV was employed for the MS analyses. Data was collected in a 5-to-7-min period of signal averaging by using precursor-ion scan mode. The scan range was 150–1300 *m/z,* and the scan rate was set as 1000 Da/s. The collision-induced dissociation (CID) gas pressure and collision energy were set at 1.0 mTorr and 40 V. The selected product ions of methyl-derivatized PIP$_2$ and PIP$_3$ used to quantify individual polyphosphoinositides were 497.1 *m/z* and 605.1 *m/z*, respectively. Data processing was performed by Xcalibur software (version 2.4, Thermo, Waltham, MA, USA). The intensity of endogenous species was corrected to that of the corresponding internal standards (giving a response ratio for each lipid).

2.9. Targeted Metabolomic Analysis

The targeted metabolomic analysis was performed as previously described [16]. Cells were washed with PBS three times and lysed in ice-cold 80% methanol/water by rapid freeze-thawing with liquid nitrogen. After centrifugation at $14,000 \times g$ for 15 min, insoluble pellets were resolved in RAPI buffer for protein determination by BCA Protein Assay Kit, and supernatants were dried down in a concentrator at 4 °C. Dried metabolite extracts were resuspended in 50% methanol/water containing internal standard (succinic acid-2,2,3,3-D4, Sigma, Darmstadt, Germany) before MS/MS analysis.

Targeted metabolomic analysis was performed on an Ultimate 3000 UHPLC system coupled with a QqQ mass spectrometer (Thermo, Waltham, MA, USA). Samples were separated on an ACQUITY UPLC BEH Amide column (2.1 × 100 mm, 1.7 μm, Waters, USA) at 30 °C column temperature at a flow rate of 0.3 mL/min. The mobile phase consisted of solvent A (10 mM NH_4Ac, 0.1% NH_4OH, water) and solvent B (10 mM NH_4Ac, 0.1% NH_4OH, ACN). The gradient settings are as follows: 0 min, 100% B; 7 min, 70% B; 9.5 min, 40% B; 12 min, 30% B; 15 min, 100% B; 20 min, 100% B. 10 μL of samples were injected. MS/MS spectra were acquired using selected reaction monitoring (SRM) mode. The used transitions for metabolites were listed in Table S1. The capillary voltage of HESI source was −2.6 kV in negative ion mode. The pressure of sheath, aux, and sweep gas flow was set as 40, 10, and 1 arbitrary unit, respectively. The capillary temperature and probe heater temperature were set as 350 °C and 320 °C. The precursor ion isolation window was set at ±0.35 *m/z* unit. The CID gas was 1.5 mTorr with a well time of 50 ms. The identification of selected metabolites was based on the precise *m/z* and retention time of chemical standards. Data were processed by Thermo Xcalibur (version 4.1). Relative metabolite levels were expressed relative to the levels of the control group after normalization to protein content. To quantify the ratio of NAD^+/NADH and ATP/ADP, absolute concentrations of these metabolites were determined using calibration curves generated with external standards of the corresponding metabolites.

2.10. Seahorse Assay

Real-time cellular bioenergetics of NR8383 cells were measured by a Seahorse XF extracellular flux analyzer (Agilent, Santa Clara, CA, USA). Briefly, cells were seeded in an XF 8-well Miniplate at a density of 40,000 cells per well and incubated overnight. Cells were treated with LPS and CEL for 2 h. After treatment, cells were washed twice and replaced with pre-warmed XF DMEM medium (bicarbonate-free, PH 7.4, Agilent, Santa Clara, CA, USA) supplemented with 10 mM glucose, 1 mM pyruvate, and 2 mM L-glutamine. Cells were then placed into a non-CO_2 incubator at 37 °C for equilibration before measuring the OCR on the Seahorse analyzer. For the Mito Stress assay, 1.5 μM oligomycin was injected first to inhibit ATP synthase following basal measurements. Next, 1 μM carbonyl cyanide-4 (trifluoromethoxy) phenylhydrazone (FCCP) was added to calculate maximal respiratory capacity. Finally, a mixture of antimycin/rotenone A, inhibitors of complex I and complex III in the respiratory chain, was injected with a final concentration of 0.5 μM to shut down mitochondrial respiration and measure nonmitochondrial respiration. For the Glycolysis Stress assay, cells are incubated in XF DMEM culture media supplemented with 2 mM L-glutamine, and the extracellular acidification rate (ECAR) is measured. The modulators in this assay, including glucose (10 mM), Oligomycin (1 μM), and 2-deoxy-glucose (2-DG, 50 mM), were serially injected into the appropriate port of the injector plate. For the real-time measurements, the values of OCR and ECAR were recorded over 80 min by running the Seahorse XFp analyzer. After assay performance, cells were counted by the Automated Cell Counter (Thermo, Waltham, MA, USA), and values were used for data normalization. The data analysis was performed by the Seahorse Wave Software (version 2.4, Agilent, Santa Clara, CA, USA).

2.11. RT-PCR Assay

Total RNA (~1 mg) was extracted using TRIzol reagents (Invitrogen, Waltham, MA, USA). cDNA was then synthesized by PrimeScript RT reagent Kit (TaKaRa, Kusatsu, Japan). qRT-PCR was performed using TB Green Premix Ex Taq Kit (TaKaRa, Kusatsu, Japan) on a PikoReal System (Thermo, Waltham, MA, USA). Relative mRNA levels were calculated using the $2^{-\triangle\triangle Ct}$ method after normalization to loading control (GAPDH) level.

2.12. Statistical Analysis

GraphPad Prism 10.0. was used for statistical analysis in this study. Statistical tests (*p*-value) for data were conducted using the two-tailed Student's *t*-test or ANOVA followed by Tukey's multiple comparison test. $p \leq 0.05$ was considered statistically significant, and statistical significance was indicated as * $p < 0.05$; ** $p < 0.01$; *** $p < 0.001$ (compared to control samples) or # $p < 0.05$; ## $p < 0.01$; ### $p < 0.001$ (compared to LPS group). Data with error bars were represented as the mean ± SD or mean ± SEM from at least three independent experiments.
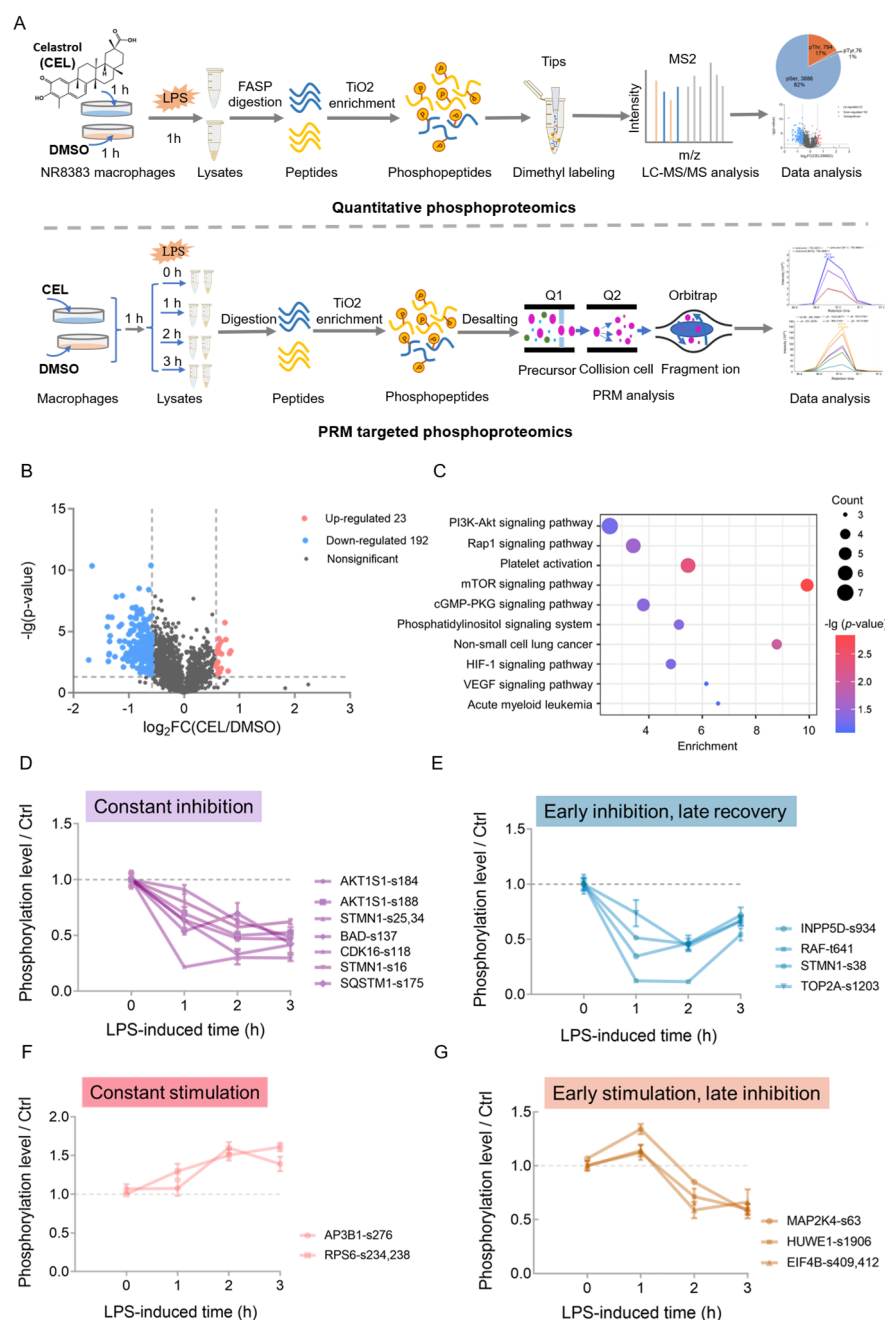
3. Results

3.1. CEL Dynamically Remodels Inflammatory Signaling Networks through Modulating Protein Phosphorylation Networks

Inflammatory response is controlled by signaling pathways coordinated by numerous interconnected kinase phosphorylation events. To elucidate the kinase networks involved in CEL-induced anti-inflammation, we employed an optimized phosphoproteomic workflow based on the dimethyl-labeling strategy to quantify site-specific phosphorylation status of protein modulated by CEL (1 µM) in NR8383 cells before LPS (100 ng/mL) stimulation at mentioned conditions (Figure 1A). The dose of CEL was determined based on previous studies, which showed that CEL at this concentration exhibited anti-inflammatory effects without causing detectable cytotoxicity in different immune cell models [17–19]. The phosphoproteomic workflow enabled the identification of 4756 phosphorylation sites on 1120 phosphoproteins (Supplementary Materials S1). Analysis of the phosphorylated amino acid distribution showed that 82% of phosphorylation sites were on serine, 17% were threonine phosphorylation sites, and only 1% were tyrosine-containing peptides (Figure S1), which underscores the general challenges in detecting them by MS. Using 1.5-fold change and adjusted $p < 0.05$ (*t*-test) as filter criteria, compared with the control group (DMSO), CEL treatment resulted in 23 up-regulated and 192 down-regulated phosphosites compared with LPS stimulation only (Figure 1B). The number of down-regulation sites was roughly 8-fold higher than up-regulated sites, which indicated that CEL affects cellular protein kinases in a short time of treatment and mainly through inhibiting LPS-induced phosphorylation. To understand the biological meaning of these significantly altered phosphoproteins, we performed the KEGG pathway analysis. CEL treatment mainly influenced immune-related pathways including PI3K/AKT, RAP1, mTOR, cGMP-PGK signaling pathway and platelet activation, etc. (Figure 1C), which confirmed the important role of CEL in immunomodulatory [20]. We then visualized phosphosite dynamic changes involving specific pathways as an integrated heatmap and found that CEL altered the phosphorylation of multiple well-known inflammation pathways, including PI3K/AKT, mTOR, VEGF, HIF-1, MAPK, and RAP1 signaling pathways (Figure S2). A particularly large number of phosphoproteins is involved in PIK3/AKT and mTOR pathways, which is consistent with previous studies showing CEL alters the PI3K/AKT signaling axis to suppress inflammatory responses [21]. Collectively, these observations revealed that the rapid anti-inflammation effect of CEL correlated with phosphorylation alterations in multiple cellular signaling pathways.

To further validate our profiling data and character dynamic phosphorylation of key notes in inflammatory signaling pathways regulated by CEL after stimulation of LPS, we expanded the LPS-stimulated time for CEL-pretreated rat macrophages including 0, 1, 2, 3 h and quantified the phosphorylation levels of selected phosphosites by Parallel reaction monitoring (PRM)-based targeted quantitative method (Supplementary Materials S2). Briefly, MS/MS spectrum of targeted phosphopeptide (e.g., AKT1S1-S183) from data-dependent acquisition (DDA) was used as a spectral library to match the fragment spectrum acquired by the PRM method (Figure S3A). All three isotopic precursors were used for identity confirmation (Figure S3B), while six top fragment ions generated from PPM were integrated for peptide abundance calculation (Figure S3C). The ion intensity of both featured fragment ions from this peptide was recorded across all samples to determine the relative abundance of targeted phosphopeptides. Despite several phosphopeptides (BAD-S135, HUWE1-S1906, AP3B1-S276, MAP2K4-S63) showing an opposite result to the profiling data as MS technical issues resulted in the truncation of some extracted PRM chromatograms [22], most of the targeted phosphopeptides showed the same phosphorylation trend as quantitative profiling (Table S2), which confirmed the reliability of our profiling data.

The temporal analysis of CEL-regulated phosphosites during LPS challenge distinguished four regulation patterns (Figure 1D–G). Most of the targeted phosphosites (AKT1S1-S184/S188, STMN1-S25,34, BAD-S137, CDK16-S118, STMN1-S16, SQSTM1-S175) were constantly inhibited by CEL during the whole time-course of LPS stimulation (Figure 1D), revealing the prominent inhibition of LPS-induced phosphorylation by CEL. The phosphorylation of INPP5D-S934, RAF1-S641, STMN1-S38, and TOP2A-S1203 was rapidly inhibited by CEL as early as 1 h following LPS stimulation and followed by a modest recovery (Figure 1E). CEL treatment progressively upregulated the phosphorylation level of AP3B1-S276 and RPS6-S234,238 in response to LPS challenge (Figure 1F). MAP2K4-S63 and EIF4B-S409,412 were slightly up-regulated by CEL after LPS stimulation for 1 h, while showing a progressive inhibition through the final time point, 3 h after stimulation of LPS (Figure 1G). Collectively, the temporally distinct phosphosite clusters revealed that CEL regulated the phosphorylation of inflammatory effectors in a time-dependent manner upon LPS stimulation. More importantly, most temporally regulated phosphoproteins had a direct or indirect relationship to PI3K/AKT/mTOR signaling pathway, master regulators of cell growth and metabolism [23,24], including its downstream target AKT1S1, the downstream effectors such as BAD, RPS6, and EIF4B, the regulator INPP5D (also known as SHIP1), the

activation marker like STMN1 and MAP2K4. Additionally, SQSTM1 and RAF have been reported to be associated with PI3K/AKT/mTOR pathway [25]. Altogether, these results suggested that PI3K/AKT/mTOR pathway was centrally positioned in CEL-regulated phosphorylation events under LPS challenge.
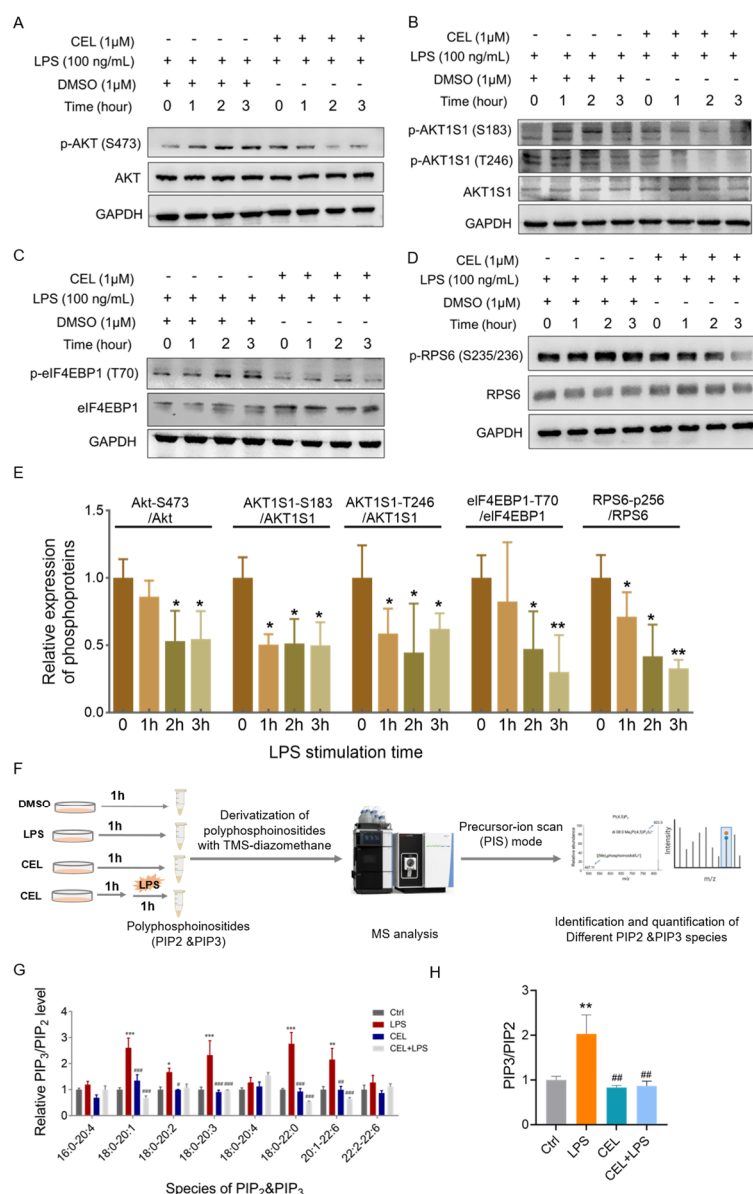

Figure 1. Phosphoproteomic analysis of NR8383 cells treated with CEL upon LPS stimulation. (**A**) Workflow of phosphoproteomic analysis; (**B**) Volcano plot of identified phosphosites by plotting the log-transformed average ratio of three replicates and *p*-value; (**C**) Bubble plot of the KEGG pathway enrichment of significantly regulated phosphoproteins by CEL. The 10 most significant pathways ($p < 0.05$) are presented on the Y-axis, and the X-axis label represents the fold enrichment of each pathway; (**D**–**G**) Time-dependent regulation of CEL-regulated phosphoproteins in NR8383 cells after stimulating with LPS for 1, 2, and 3 h. Values are normalized to their respective 0-h time point after calibrating by a housekeeping gene (GAPDH) and represented as means ± SEM of three independent experiments.

3.2. CEL Suppresses PI3K/AKT/mTOR Signaling and PIP3 Accumulation

To evaluate whether PI3K/AKT/mTOR pathway is involved in the inhibition of LPS-induced inflammation by CEL, we performed the western-blot analysis to examine the temporal phosphorylation of key pathway components of PI3K/AKT and mTOR. Notably, LPS stimulated robust phosphorylation of AKT S473 and its well-

recognized classical downstream target AKT1S1 T246, whereas this response was completely blocked by CEL in a time-dependent manner (Figure 2A,B,E). We also detected S183 (S184 in rat) phosphorylation of AKT1S1, a mTORC1-activity indicator site, which increased in response to LPS stimulation but was alleviated by pretreatment of CEL (Figure 2B,E), which was consistent with the observation in targeted PRM analysis. Additionally, LPS-induced mTOR activation as evidenced by temporally elevated phosphorylation of eIF4EBP1 T70 and RPS6 S235/236, frequently used surrogate readouts for mTORC1 activity, whereas this activation was consistently inhibited by CEL (Figure 2C–E). Consequently, we proposed that CEL elicited the rapid anti-inflammation effect predominantly by inhibition of phosphorylation of PI3K/AKT/mTOR signaling pathway.

Figure 2. Effect of CEL on PI3K/AKT/mTOR pathway protein expression and phosphoinositide abundance. (**A–D**) Immunoblot analysis of specified phosphoproteins in NR8383 cells after stimulation with LPS for the indicated time points with pre-treatment of CEL. (**E**) Quantitative results of western-blot assay for phosphoproteins. GAPDH was used as a loading control. Data are normalized to the control sample at 0 h and presented as mean ± SD of three biological replicates. Statistical significance was calculated using one-way ANOVA with Tukey's multiple-comparison test compared to the 0-h time point of LPS stimulation, which was indicated as * p-value < 0.05, ** p-value < 0.01. (**F**) The workflow of MS-based lipidomic analysis of PIP2 and PIP3 species. (**G,H**) The relative level of individual (**G**) and total (**H**) PIP2 and PIP3 species in NR8383 cells with treatment of CEL and LPS. The fold change is obtained by calculating the response ratio of each molecular species of PIP3 divided by that of its respective PIP2 species. Data are presented as mean ± SEM of three biological replicates. * p < 0.05, ** p < 0.01, *** p < 0.001 (* significant changes compared to control samples), # p < 0.05, ## p < 0.01, ### p < 0.001 (# significant changes compared to LPS group).
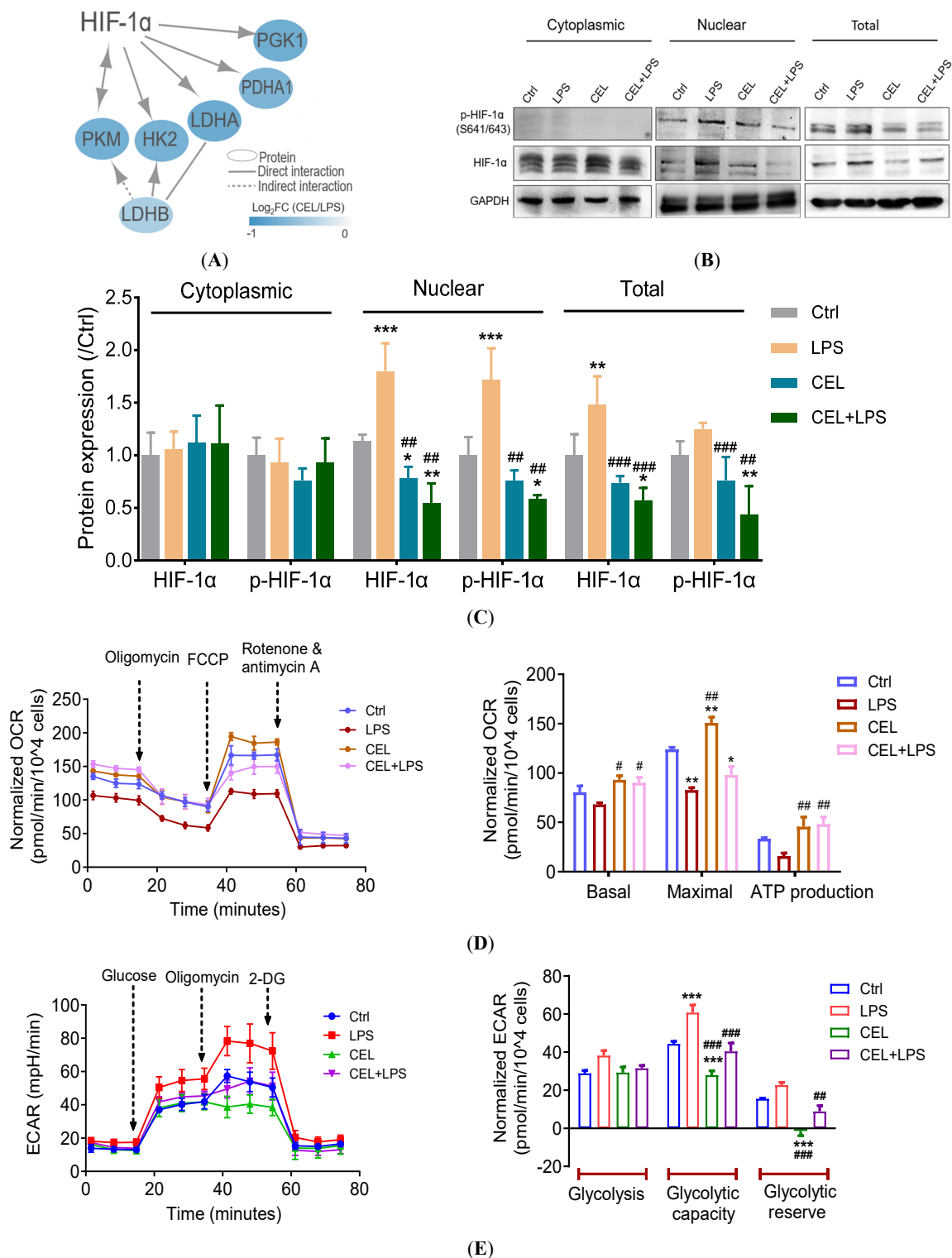
Activated PI3K converts phosphoinositide 4,5-bisphosphate (PIP2) to phosphatidylinositol (3,4,5)-triphosphate (PIP3), and the PI3K-induced PIP3 generation leads to AKT and mTOR pathway activation. To further examine the effect of CEL on PIP2 and PIP3 levels in macrophages in response to LPS stimulation, we applied an optimized MS-based method to quantify the abundance of several species of PIP2 and PIP3 (Figure 2F). Given the very low levels of PIP2 and PIP3 in the cells and to quantify more species with different fatty acyl chains, we performed a comprehensive analysis of individual PPI isomers in the presence of internal standards (IS) using lithium adducts of methylated PIP2 and PIP3 species in precursor-ion scanning (PIS) mode based on a previously published article [26]. The identification of methylation-derived PIP2 and PIP3 species was confirmed by the MS/MS spectra of the corresponding IS shown in Figure S4A,B). We successfully quantified 18 PIP2 and 14 PIP3 species, respectively (Figure S4C,D) & Supplementary Materials S3. The ratio of PIP3 to PIP2 reflects the relative accumulation of PIP3 in cells upon stimuli, which was calculated by the quantification results of individual PIP2 and PIP3 species with the same fatty acid chains as shown in Figure 2G. We found that LPS stimulation significantly increased the ratio of PIP3/PIP2 in most of quantified PIP3/PIP2 species, suggesting that PIP3 generation activates AKT, further confirming our previous WB results that LPS stimulation activates the PI3K-AKT signaling pathway. By contrast, CEL pretreatment significantly inhibited the LPS-induced PIP3 accumulation with a relatively lower PIP3/PIP2 ratio than LPS, which suggested that CEL treatment can inhibit the activation of PI3K/AKT pathway induced by LPS stimulation. We also combined the abundance of all detected PIP3 and PIP2 species to obtain an overall change in the PIP3/PIP2 ratio with the treatment of CEL and LPS. As shown in Figure 2H, we yielded a similar result that CEL pretreatment markedly reduced LPS-induced PIP3 production. Taken together, these results suggested CEL suppresses inflammatory response by inhibiting PI3K/AKT/mTOR signaling pathway and PIP3 accumulation.

3.3. CEL Facilitates Metabolic Shift from Glycolysis to Mitochondrial Respiration by HIF-1α Inactivation

Pro-inflammatory stimuli, including LPS, activate macrophages, prompting them to undergo metabolic reprogramming to meet the energy and biosynthetic demands associated with inflammatory responses. HIF-1α activation is highly dependent on activation of the PI3K/AKT/mTOR pathway [27], which further promotes macrophage metabolic reprogramming in hypoxic or inflammatory conditions[12]. In addition, we found that the HIF signaling pathway was significantly enriched (Figure 1C) and multiple key downstream metabolic regulators of HIF-1α, including PKM, HK2, LDHA, PDHA1, PGK1, and LDHB, were regulated by CEL treatment from our quantitative proteomics data (Supplementary Materials S4 & Figure 3A). These data collectively indicated that CEL may affect macrophage metabolic reorganization under LPS-induced inflammatory conditions by the regulation of HIF-1α. The nuclear accumulation of stabilized HIF-1α is necessary for it to act as a transcription factor to regulate the downstream metabolic pathways [28], and the nuclear localization and transactivity of HIF-1α were reported to be highly affected by HIF-1α protein phosphorylation [29]. To verify whether nuclear accumulation and activity of HIF-1α are affected by CEL, we detected the phosphorylation and protein expression of HIF-1α in macrophage cytoplasmic, nuclear, and total extracts with the treatment of CEL and LPS stimulation. As shown in Figure 3B,C, LPS stimulation significantly increased the phosphorylation level of HIF-1α S641/643 with an elevated protein expression of HIF-1α in both the nuclear and total extracts compared with the control group, while no obvious changes of HIF-1α phosphorylation and protein expression were observed in cytosolic extracts. As expected, the nuclear localization and activity of HIF-1α were highly correlated with the phosphorylation of S641/643, and the elevated nuclear accumulation induced by LPS also indicated an enhanced transcriptional activity of HIF-1α as previously reported [29]. However, pretreatment of CEL reversed this effect; the phosphorylation and protein expression of HIF-1α were decreased by CEL after LPS stimulation in both the nuclear and total extracts without obvious difference among all treatment groups observed in cytosolic extracts, which suggested that CEL can suppress HIF-1α activity in LPS-activated macrophages.

Since it is well known that HIF-1α is a master regulator of macrophage metabolic reprogramming, we investigate the functional metabolic alterations regulated by CEL in LPS-challenged macrophages using a Seahorse XF-analyzer. HIF-1α stabilization reduces oxidative phosphorylation (OXPHOS) and increases glycolysis in inflammatory macrophages [30]. Indeed, in line with the increased HIF-1α stabilization (Figure 3B), we observed a decreased OXPHOS with lower basal respiration, ATP production, and maximal respiration capacity as measured by oxygen consumption rate (OCR), and an upregulated glycolysis with higher glycolytic capacity and reserve as measured by extracellular acidification rate (ECAR) in LPS-stimulated inflammatory macrophages (Figure 3D,E). In sharp contrast, CEL treatment reversed the attenuation of OXPHOS and the increase in glycolysis, increasing the basal and maximal respiration capacity and ATP production, and reducing glycolytic capacity and reserve (Figure 3D,E). Supported by the decreased HIF-1α stabilization in macrophages by CEL in
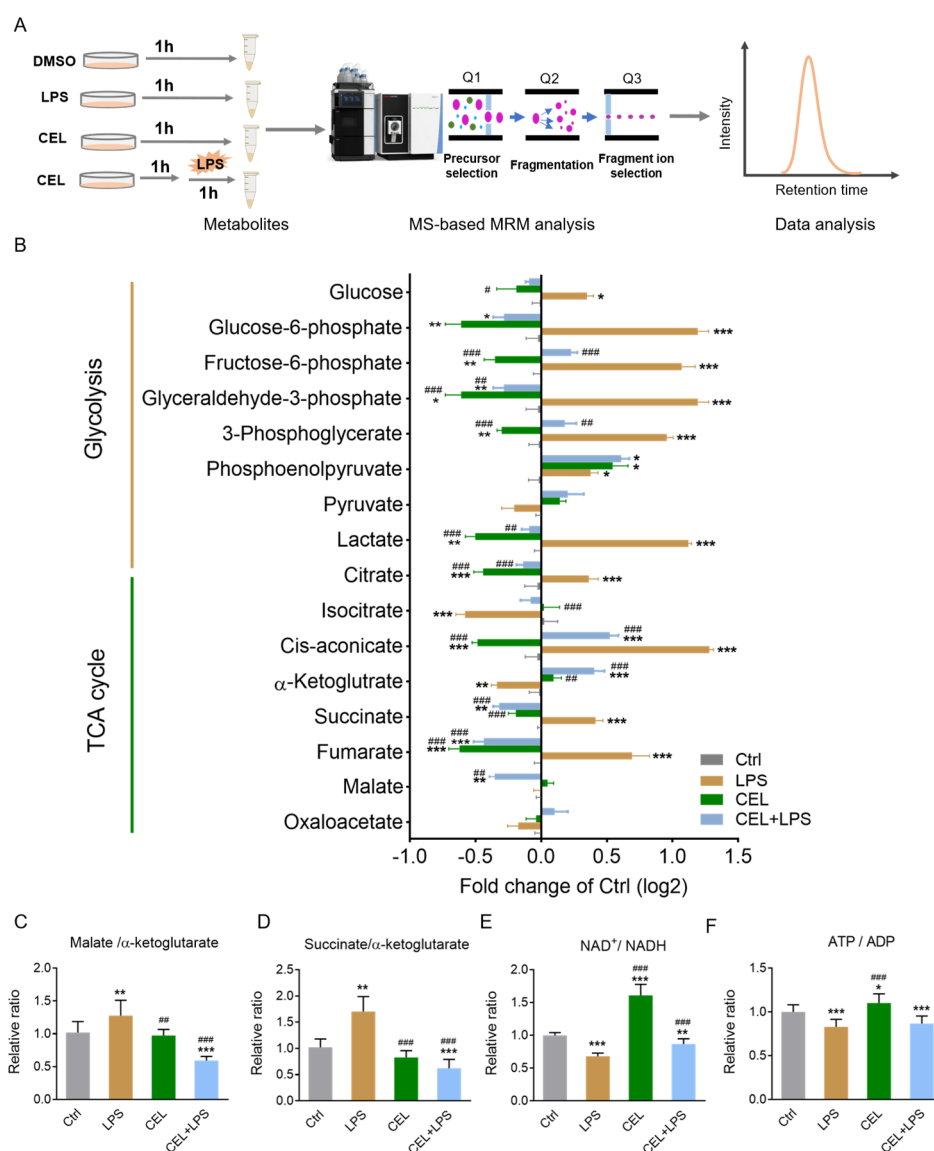
response to LPS stimulation, we thus proposed that CEL promotes dramatic metabolic reprogramming by impairing glycolytic metabolism and improving OXPHOS through regulating HIF-1α activity in LPS-activated macrophages.

Figure 3. Effect of CEL on HIF-1α activity and HIF-1α-dependent metabolic reprogramming in LPS-activated macrophages. (**A**) CEL specifically regulates HIF-1α downstream metabolic targets. (**B**,**C**) Western-blot bands and quantitative results of HIF-1α and phosphorylated HIF-1α expression at cytoplasmic, nuclear, and total levels. Data are expressed as mean ± SD (n = 3). (**D**) Mitochondrial respiratory profiles (OCR) and respiratory parameters of NR8383 cells with treatments of CEL and LPS. (**E**) Extracellular acidification profiles and glycolytic parameters of NR8383 cells, differential treatment of CEL and LPS. All values of profiles and related parameters are normalized by the number of cells after running the test. Data are expressed as mean ± SEM (n = 3). * $p < 0.05$, ** $p < 0.01$, *** $p < 0.001$(* significant changes compared to control samples), # $p < 0.05$, ## $p < 0.01$, ### $p < 0.001$ (# significant changes compared to LPS group).

3.4. CEL Restores TCA Cycle Integrity and Cellular ENERGY Balance

To further explore the detailed changes in metabolic pathways and the possible metabolites involved, we quantified the cellular metabolites of glycolysis and TCA cycle with the treatment of CEL and LPS by MS-based targeted metabonomic analysis (Figure 4A). As shown in Figure 4B, LPS stimulation resulted in increased cellular levels of major glycolytic intermediates, including glucose, G6P (glucose-6-phosphate), F6P (fructose-6-phosphate), GADP (glyceraldehyde-3-phosphate), 3PG (3-phosphoglycerate), PEP (phosphoenolpyruvate) and lactate, compared to control samples, which is consistent with preceding work that indicated glycolysis is increased with HIF-1α activation in response to LPS stimulation [31,32]. Conversely, CEL treatment significantly decreased the levels of the indicated glycolytic intermediates in unstimulated macrophages and markedly reduced the increased intermediates by LPS stimulation. This result is in line with our findings in proteomics analysis, CEL decreased essential glycolysis proteins such as HK2, PKM, LDHA, PDHA1, PGK1, and LDHB, the main glucose transporter, in LPS-stimulated macrophages (Figure 4B). Hence, CEL treatment can reverse the elevated glycolysis regulated by HIF-1α in LPS-stimulated macrophages.
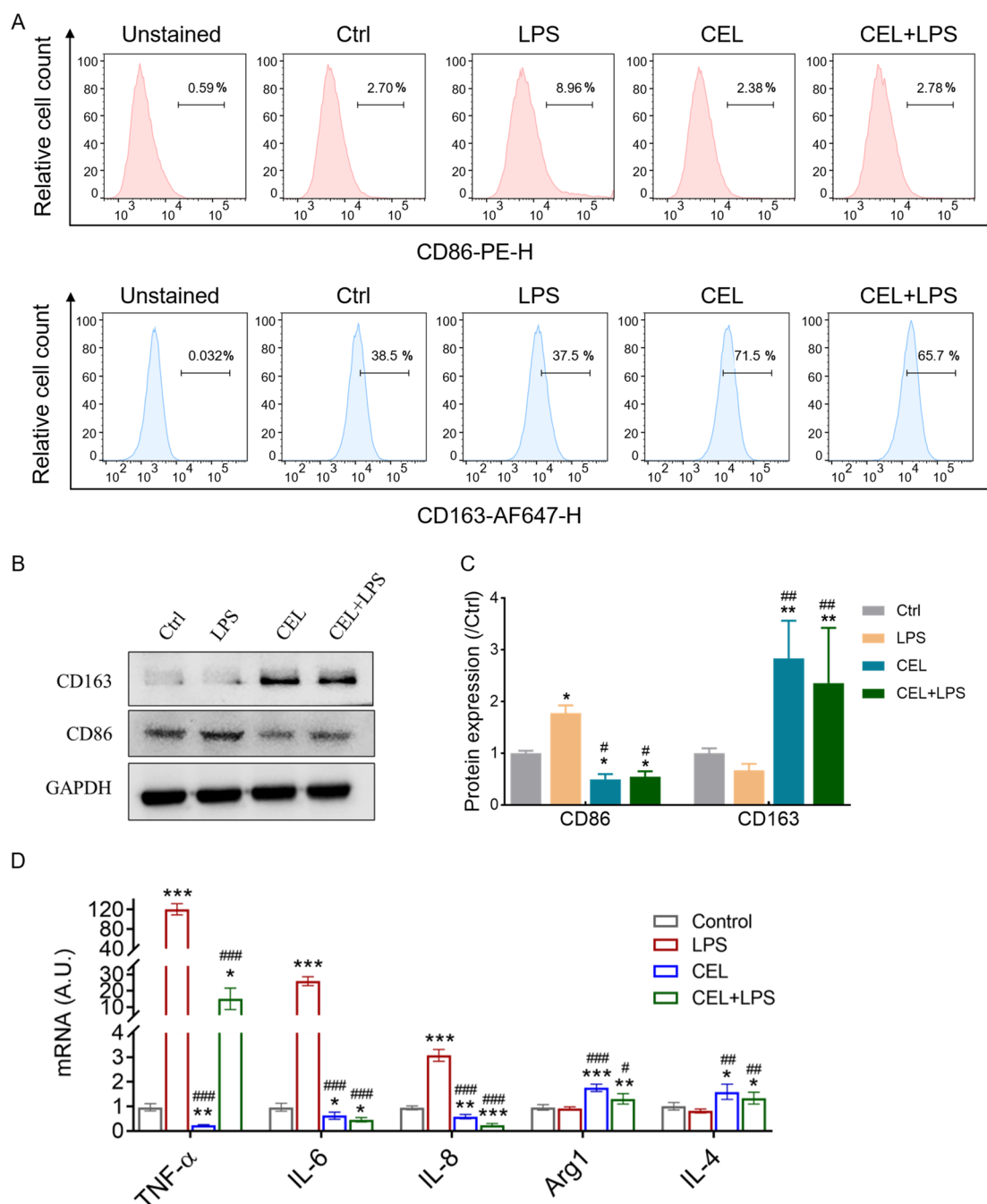

Figure 4. Targeted analysis of CEL-mediated metabolites in glycolysis and TCA cycle. (**A**) Workflow of MS-based targeted metabonomic analysis. (**B**) Relative metabolite levels of glycolysis and TCA cycle pathway in NR8383 cells with treatment of CEL and LPS. Data are normalized to internal standard and protein content and presented relative to the respective level of the control group. (**C,D**) The ratio of malate/α-ketoglutarate and succinate/α-ketoglutarate. Results were shown as mean ± SEM (n = 10). (**E,F**) The ratio of NAD/NADH and ADP/ATP was represented with fold change between the experimental and control groups. Error bar of each bar graph represents mean ± SD (n = 15). * $p < 0.05$, ** $p < 0.01$, *** $p < 0.001$(* significant changes compared to control samples), # $p < 0.05$, ## $p < 0.01$, ### $p < 0.001$ (# significant changes compared to LPS group).

We next analyzed the relative levels of TCA cycle metabolites in macrophages with the treatment of CEL after LPS stimulation (Supplementary Materials S5). Except α-ketoglutarate and isocitrate, we observed a global increase in TCA cycle metabolites in response to LPS (Figure 4B). In contrast, CEL treatment showed an opposite regulation pattern with reduced cellular concentrations of citrate, cis-aconitate, succinate, and fumarate and elevated a-ketoglutarate and isocitrate levels. We did not observe significant changes in malate levels in LPS-stimulated macrophages, the downstream metabolites of α-ketoglutarate, while an elevated malate to α-ketoglutarate ratio was found upon LPS stimulation (Figure 4C). The ratio of malate to α-ketoglutarate reflects the relative contribution of the TCA cycle to the pool of malate. This increased ratio was significantly inhibited by CEL treatment, suggesting a block in the TCA cycle between α-ketoglutarate and malate in CEL-treated macrophages with LPS stimulation. The accumulation of succinate with a reduction of α-ketoglutarate indicated a break in the TCA cycle in LPS-activated macrophages, which is a key event during the metabolic reprogramming process in inflammatory macrophages [33]. To further verify this, we also calculated the ratio of succinate to α-ketoglutarate, which is reported to be important in determining the phenotypic state of macrophages. Our data showed a significant increase in succinate to α-ketoglutarate ratio induced by LPS stimulation, and CEL treatment led to a reduction of LPS-induced increased ratio (Figure 4D). The transient high succinate to α-ketoglutarate ratio was reported to increase the stability of HIF-1α [9]. Indeed, a similar pattern of regulation of HIF-1α protein expression is observed as the ratio of succinate to α-ketoglutarate. These results collectively suggested that CEL treatment blocked the α-ketoglutarate leakage to ensure that intermediates were available for the TCA cycle, contributing to improving mitochondrial oxidation. Given the vital roles of ATP/ADP and NAD$^+$/NADH balance in macrophage metabolic reprogramming, we measured the ratios of ATP/ADP and NAD$^+$/NADH by their absolute concentrations in macrophages with the treatment of CEL and LPS (Supplementary Materials S6), to obtain a more comprehensive view of the role of CEL in macrophage metabolic reprogramming. A reduced NADH/NAD$^+$ ratio in LPS-activated macrophages (Figure 4E) reflected an increased α-ketoglutarate flux into the TCA cycle as observed in Figure 4B via the inhibition of isocitrate dehydrogenase activity [34]. This reduced NADH/NAD+ ratio was then reversed by CEL treatment, suggesting that CEL may mitigate the disruption of TCA cycle in LPS-activated macrophages by reducing NADH/NAD$^+$ levels. Furthermore, LPS decreased the ATP/ADP ratio reflecting a high demand for ATP in activated macrophages (Figure 4F), which is consistent with a shift from ATP synthesis by oxidative phosphorylation to ATP synthesis by glycolysis. CEL treatment elevated the reduced ratio of ATP/ADP, indicating that CEL partially compensates for the energy requirements of metabolic reprogramming during macrophage activation. Together, these results indicated that CEL regulates macrophage metabolic reprogramming by reducing glycolysis and blocking TCA fragmentation in a HIF-1α-dependent manner.

3.5. Metabolic Rewiring Underpins CEL-Induced Anti-Inflammatory Macrophage Polarization

Metabolic rewiring has been closely associated with macrophage polarization to exhibit distinct functional phenotypes. To evaluate the effect of CEL on macrophage polarization, we examined the expression of typical markers of M1/M2-like macrophages with the treatment of CEL and LPS challenge. As shown in Figure 5A, compared to the control samples, LPS stimulation significantly increased the flow cytometric signal of CD86, a typical marker of M1 macrophages, while this change was normalized by CEL treatment. Although we did not observe any significant difference in the fluorescence signal of CD163, a marker of M2-like macrophages, between LPS treatment and control, CEL treatment markedly elevated the fluorescence signal of CD163 with or without LPS stimulation. To verify this finding, we detected the protein expression of CD86 and CD163 by western blotting assay and finally obtained a similar result. CEL treatment suppressed the increased CD86 expression induced by LPS challenge and enhanced the expression of CD163 (Figure 5B,C). In addition, the mRNA levels of several representative M1/M2 polarization-related markers were measured to confirm the role of CEL in mediating macrophage polarization (Table S3). As a result, LPS stimulation led to a dramatic upregulation of the mRNA expression of proinflammatory M1 marker genes, including TNF-α, IL-6, and IL-8, but this effect was suppressed by CEL treatment with significantly lower mRNA levels in indicated genes than those of the LPS group (Figure 5D). Furthermore, consistent with the increased CD163 expression, CEL significantly elevated the expression of anti-inflammatory M2-like markers including Arg1 and IL-6 with or without LPS stimulation (Figure 5D). Taken together, these results suggested that CEL elicited a phenotypic switch from M1-like type to M2-like type in LPS-stimulated macrophages.

Figure 5. Effects of CEL on M1/M2 polarization-related markers. (**A**–**C**) Flow cytometric (**A**), western blot analysis (**B**), and the corresponding quantitative results (**C**) of M1/M2 polarization-related markers (CD86 for M1, CD163 for M2) in NR8383 cells with or without treatment of CEL and LPS. (**D**) mRNA levels of M1/M2 polarization-related marker in NR8383 cells with or without treatment of CEL and LPS. The mRNA levels of detected genes were converted to arbitrary units, normalized to the value of the control group after calibrating by a housekeeping gene (GAPDH). Two-way ANOVA with Tukey's multiple comparisons is used to calculate *p*-value. * $p < 0.05$, ** $p < 0.01$, *** $p < 0.001$(* significant changes compared to control samples), # $p < 0.05$, ## $p < 0.01$, ### $p < 0.001$ (# significant changes compared to LPS group).

4. Discussion

Although the anti-inflammation effect of CEL has been widely reported, its molecular target and the underlying mechanism are still largely unclear. Here, we showed that CEL suppresses inflammatory response in LPS-activated macrophages by modulating PI3K/AKT/mTOR pathway in a time-dependent manner. Furthermore, CEL mediated macrophage metabolic remodeling by reversing LPS-induced enhanced glycolysis and disrupting OXPHOS and TCA cycling, and this effect was dependent on HIF-1α activation. Thus, our multi-omics analysis

suggested that CEL regulated macrophage metabolic reprogramming through PI3K/AKT/mTOR/HIF-1α axis, providing a rational explanation for the rapid anti-inflammatory effect of CEL.

CEL has been shown to have anti-inflammatory therapeutic potential by modulating multiple signaling pathways involved in the inflammatory response, including NF-Kb [35], PI3K/AKT/mTOR [36], and Nur77-dependent pathway [36]. However, the comprehensive landscape of the dynamics of CEL-mediated signaling networks of acute inflammatory response is still limited. Our phosphoproteomic profiling data captured hundreds of altered components involved in multiple well-known inflammatory responses, indicating the remodeling of complex signaling networks involved in the rapid anti-inflammatory activity of CEL. Further time-resolved targeted PRM and western blotting validation effectively captured dynamic kinase signaling alterations and revealed PI3K/Akt/mTOR as a central target of CEL, strengthening causality beyond static analyses. In addition, by layering targeted lipidomics, we successfully quantify the specific upstream lipid second messengers, which are the direct products and regulators of PI3K activity [37]. We not only revealed changes in PIP3 abundance but also found that CEL significantly altered specific PIP2 and PIP3 isoforms with different acyl chains. These data suggested a potentially novel regulatory mechanism that the acyl chain composition of phosphatidylinositol could finely regulate signalling output, providing new clues for exploring the functional specificity of lipid species in inflammation. The integrated phosphoproteomics and metabolomics data revealed the crosstalk of PI3K/Akt/mTOR signaling and the downstream metabolic consequences (inhibited glycolysis and TCA restoration) with HIF-1α as a key linkage in CEL-regulated inflammatory response. Therefore, compared to previous studies, our data provided a comprehensive insight into dynamics of CEL-regulated signaling-metabolic reprogramming networks to identify central molecular circuits in complicated biological systems, such as inflammatory responses.

Phospholipids, such as phosphatidic acid and lysophosphatidic acid, are known to influence inflammatory signaling and mTOR activation [38,39]. However, in this study, we specifically targeted PIP2 and PIP3, the direct substrates of PI3K enzymes, which are believed to rapidly and temporarily remodel cellular functions by modifying enzymatic activity [40]. There is increasing evidence that differential acyl chains can affect the regulation and function of PIP2 and PIP3 [41,42]. Specifically, polyunsaturated PIP2 subspecies (e.g., PIP2 C18:0–20:4) are the preferred substrates for phospholipase C. Their hydrolysis generates second messengers, including IP3, a potent regulator of mitochondrial metabolism and TCA cycle enzymes, and Diacylglycerol (DAG). The fatty acyl composition of DAG determines its ability to activate specific isozymes of protein kinase C, which have diverse roles in regulating glucose uptake and cell growth [43–45].Additionally, polyunsaturated lipids have been shown to promote membrane deformation and fission by adjusting the conformation to the actual curvature of the membrane [46]. This enhanced flexibility may further amplify the amplitude and duration of downstream signaling pathways (e.g., PI3K-AKT pathway), triggering subsequent metabolic reprogramming of macrophages. Although more evidence is needed, considering PIP2 and PIP3 as upstream membrane molecules of the PI3K/AKT/mTOR signaling pathway, the significantly changed PIP2 and PIP3 species identified in this study may be indicators of the fast inflammatory response in macrophages, as well as potential targets of CEL.

HIF-1α, as the downstream target of PI3K/AKT/mTOR signaling pathway, stabilizes and aggregates in the nucleus to facilitate the control of genes involved in cellular metabolism [28]. The stability and activity of HIF-1α are highly influenced by protein post-translational modifications [47]. Consistent with previous studies [48,49], we demonstrated the activation of HIF-1α in LPS-activated macrophages characterized by a significant increase of HIF-1α protein expression and phosphorylation in nuclear and total lysates. This HIF-1α accumulation was significantly suppressed by CEL treatment, suggesting the inhibitory effect of CEL on HIF-1α activation. CEL has been widely reported to strongly inhibit HIF-1α activity in cancer cells [50,12], while our data demonstrated that CEL could also be an inhibitor of HIF-1α in LPS-stimulated macrophages. Given the critical role of HIF-1α in macrophage metabolic reprogramming [12,51], we reasoned that CEL might mediate macrophage metabolic remodeling by targeting HIF-1α. Indeed, we observed an enhanced glycolytic metabolism and impaired OXPHOS in activated macrophages, which has been well-documented to be regulated by macrophage HIF-1α [11,30]. This metabolic switch was reversed upon treatment with CEL, confirming the central role of HIF-1α in CEL-mediated metabolic remodeling.

In LPS-stimulated macrophages, another typical alteration in metabolic status is marked by broken TCA cycle with the accumulation of citrate and succinate, as shown in Figure 4. Macrophage citrate and succinate were reported to be modulated by HIF-1α [52]. In turn, succinate further enhanced HIF-1α activity and potentiated inflammatory responses [30]. Activated macrophages, especially those polarizing towards an M1 phenotype, require more ATP, and this high energy demand can lead to enhanced TCA cycle activity and a lower $NADH/NAD^+$ ratio, which we observed in LPS-stimulated macrophages. In addition, a decrease in $NADH/NAD^+$ ratio was reported to enhance HIF-1α activity through the SIRT1 pathway under hypoxic conditions [53]. In this

context, suppressed glycolysis and TCA breakage by CEL may depend on the inhibition of HIF-1α activity. We also demonstrated that in LPS-activated macrophages, CEL facilitated a phenotypic switch from M1 to M2 characterized by inhibition of pro-inflammatory M1 marker expression and elevation of anti-inflammatory M2 marker expression. HIF-1α was suggested to be involved in M1/M2 phenotypic switch in a response dependent on glycolytic genes and inflammatory cytokines [54]. Furthermore, targeting macrophage HIF-1α has been shown to ameliorate inflammation and may be a promising strategy for the treatment of aortic dissection, an inflammatory disease [31]. We therefore believed that remodeling the metabolic status of macrophages by pharmacological targeting of the CEL-HIF-1α axis may be a potential strategy to alleviate various pathologies associated with inflammation.

Although the use of specific PI3k inhibitors or binding assays is considered to be an effective way for identifying target regulatory effects of CEL on the PI3K/AKT/mTOR pathway, we would like to highlight that the evidence presented in our manuscript strongly supports the core role of this pathway in CEL-regulated inflammatory response. The targeted MS-based lipidomics successfully quantified 18 PIP2 and 14 PIP3 species (Figure S4C,D), and the significant reduction in the PIP3/PIP2 ratio (Figure 2G) provided direct functional evidence of PI3K inhibition by CEL. This data may be a strong surrogate for an in-cell kinase assay. In addition, the time-resolved PRM and WB analyses showed the subsequent rapid and potent dephosphorylation of the downstream cascade (AKT, RPS6 and 4E-BP1), which was consistent with the upstream inhibition of PI3K. Furthermore, our multi-omics data revealed that CEL not only inhibited the PI3K/AKT/mTOR signaling pathway but also dominated the metabolic switch from glycolysis to OXPHOS in macrophages and repaired TCA cycle disruption. In contrast, most synthetic PI3K inhibitors were not designed or known to directly correct the immunometabolic defect in macrophages, which is increasingly recognized as a fundamental driver of inflammation [55]. Compared to traditional PI3K inhibitors, CEL may be more efficacious in the treatment of complex inflammatory diseases involving the signaling-reprogramming crosstalk. This has made CEL an attractive pharmaceutical candidate for inflammatory diseases with a significant metabolic component, such as rheumatoid arthritis [2] and obesity [1]. While we have identified the PI3K/HIF-1α pathway as the core signalling pathway for its anti-inflammatory effects, the exact primary molecular targets of CEL are still not fully defined. This contrasts with synthetic inhibitors, which have been developed by engineering binding sites against specific known targets. Therefore, we would suggest that CEL should not be considered as a direct competitor to synthetic PI3K inhibitors, but rather as a different class of therapeutic agent. Its future development may lie mainly as a lead compound for the treatment of metabolism-driven inflammatory diseases.

Our study is limited, as data were obtained in a single macrophage model. Although the NR8383 cells are a well-established and relevant model for studying inflammatory responses, and have been used extensively in similar pharmacological studies [56–58]. Further validations of the mechanism of CEL-regulated inflammatory response should be performed in additional macrophage and animal models. Moreover, the interaction between CEL and PI3K will be further explored using specific PI3K inhibitors and binding assays. However, we would still like to emphasize that the depth of our omics analysis provides a strong and testable framework for future validation in other systems.

5. Conclusions

In summary, we established a landscape of dynamic functional modules and signaling networks regulated by CEL in LPS-activated macrophages by quantitative phosphoproteomics, combined with targeted lipidomic analysis of PIP2 and PIP3 species. The PI3K/AKT/mTOR pathway was identified as the central signaling pathway in CEL-mediated inflammatory response. We further found that CEL suppressed HIF-1α activity, the downstream regulator of PI3K/AKT/mTOR pathway, orchestrating metabolic reprogramming by inhibiting glycolysis and enhancing OXPHOS. Targeted metabolomics corroborated these findings, demonstrating CEL-driven suppression of glycolytic metabolites and restoration of TCA cycle integrity. Thus, for the first time, multi-omics analyses were integrated to dissect CEL's HIF-1α-mediated metabolic reprogramming, providing valuable perspectives for crosstalk between signalling and metabolic pathways in inflammatory responses.

Supplementary Materials: The following supporting information can be downloaded at: https://media.sciltp.com/articles/others/2601080931343213/HM-2508000226-Supplementary-Material.zip. Figure S1. Distribution of phosphorylated amino acids, serine (pSer), threonine (pThr), and tyrosine (pTyr) sites. Figure S2. Profile of site phosphorylation on proteins involved in different signaling pathways regulated by CEL upon LPS stimulation. Figure S3. PRM targeted quantification of a selected phosphopeptide (AKT1S1-s183). (A) MS/MS fragmentation spectra and peak area contributions of selected phosphopeptide SLPVSVPVWAFK (*m/z* 705.3651, 2+). Dot product (dotp) value indicates the degree of the match between spectral library MS/MS and the targeted ion chromatograms (B) Precursor constituent of selected phosphopeptide. (C) PRM transitions used for quantification of SLPVSVPVWAFK, mass measurement error and retention time of the most intense transition is annotated above the peak. Figure S4. Quantification of PIP2 and PIP3 species in NR8383 cells with the treatment of CEL and LPS stimulation. (A,B) MS/MS characterization of methylation-derived PIP2 and PIP3 species in the precursor-ion scanning (PIS)

mode. (A) The PIS spectrum of methylated internal standard of PIP2 species (di 08:0 PI(4,5)P2) containing 5 methyl groups in the presence of LiCl. (B) The PIS spectrum of methylated internal standard of PIP3 species (17:0−20:4 PI(3,4,5)P3) containing 7 methyl groups in the presence of LiCl. (C,D) Quantification of the molecular species of PIP2 and PIP3 species in NR8383 cells were untreated (Ctrl) or pretreated for 1 h with CEL (1 μM) before being stimulated with LPS (100 ng/mL) for 2 h. The levels of PIP2 (C) and PIP3 (D) species are determined by normalizing to the selected internal standards. Data are presented as mean ± SEM of three biological replicates, $*p < 0.05$, $**p < 0.01$, $*** p < 0.001$(* significant changes compared to control group), $\# p < 0.05$, $\#\# p < 0.01$, $\#\#\# p < 0.001$ (# significant changes compared to LPS group). Table S1. SRM transitions for targeted metabolites. Table S2. Comparison of Dimethyl labeling and PRM quantitative result of CEL-regulated phosphopeptides. Table S3. The primers for qRT-PCR.

Author Contributions: G.X.: Conceptualization, Investigation, Methodology, Data Curation, Writing—Original Draft Preparation; X.D.: Data Curation, Methodology; X.S.: Software, Methodology; L.Z. (Li Zhong): Methodology; L.Z. (Lin Zhu): Conceptualization, Data Curation, Writing—Review and Editing; Z.C.: Supervision, Validation, Writing—Review and Editing. All authors have read and agreed to the published version of the manuscript.

Institutional Review Board Statement: Not applicable.

Informed Consent Statement: Not applicable.

Data Availability Statement: All data reported in this paper will be available by the corresponding author upon request.

Conflicts of Interest: Given the role as Editorial Board Member, Zongwei Cai had no involvement in the peer review of this paper and had no access to information regarding its peer-review process. Full responsibility for the editorial process of this paper was delegated to another editor of the journal.

Use of AI and AI-Assisted Technologies: No AI tools were utilized for this paper.

Reference

1. Liu, J.; Lee, J.; Hernandez, M.A.S.; Mazitschek, R.; Ozcan, U. Treatment of Obesity with Celastrol. *Cell* **2015**, *161*, 999–1011.
2. An, L.; Li, Z.; Shi, L.; Wang, L.; Wang, Y.; Jin, L.; Shuai, X.; Li, J. Inflammation-Targeted Celastrol Nanodrug Attenuates Collagen-Induced Arthritis through NF-KB and Notch1 Pathways. *Nano Lett.* **2020**, *20*, 7728–7736.
3. Ma, X.; Xu, L.; Alberobello, A.T.; Gavrilova, O.; Bagattin, A.; Skarulis, M.; Liu, J.; Finkel, T.; Mueller, E. Celastrol Protects against Obesity and Metabolic Dysfunction through Activation of a HSF1-PGC1α Transcriptional Axis. *Cell Metab.* **2015**, *22*, 695–708.
4. Cascão, R.; Vidal, B.; Raquel, H.; Neves-Costa, A.; Figueiredo, N.; Gupta, V.; Fonseca, J.E.; Moita, L.F. Effective Treatment of Rat Adjuvant-Induced Arthritis by Celastrol. *Autoimmun. Rev.* **2012**, *11*, 856–862.
5. Luo, D.; Guo, Y.; Cheng, Y.; Zhao, J.; Wang, Y.; Rong, J. Natural Product Celastrol Suppressed Macrophage M1 Polarization against Inflammation in Diet-Induced Obese Mice via Regulating Nrf$_2$/HO^{-1}, MAP Kinase and NF-KB Pathways. *Aging* **2017**, *9*, 2068–2081.
6. Park, M.D.; Silvin, A.; Ginhoux, F.; Merad, M. Macrophages in Health and Disease. *Cell* **2022**, *185*, 4259.
7. Russell, D.G.; Huang, L.; VanderVen, B.C. Immunometabolism at the Interface between Macrophages and Pathogens. *Nat. Rev. Immunol.* **2019**, *19*, 291–304.
8. Navegantes, K.C.; Souza Gomes, R.; Pereira, P.A.T.; Czaikoski, P.G.; Azevedo, C.H.M.; Monteiro, M.C. Immune Modulation of Some Autoimmune Diseases: The Critical Role of Macrophages and Neutrophils in the Innate and Adaptive Immunity. *J. Transl. Med.* **2017**, *15*, 36.
9. Liu, P.S.; Wang, H.; Li, X.; Chao, T.; Teav, T.; Christen, S.; DI Conza, G.; Cheng, W.C.; Chou, C.H.; Vavakova, M.; et al. α-Ketoglutarate Orchestrates Macrophage Activation through Metabolic and Epigenetic Reprogramming. *Nat. Immunol.* **2017**, *18*, 985–994.
10. Putnam, K.; Shoemaker, R.; Yiannikouris, F.; Cassis, L.A. The Renin-Angiotensin System: A Target of and Contributor to Dyslipidemias, Altered Glucose Homeostasis, and Hypertension of the Metabolic Syndrome. *Am. J. Physiol. Heart Circ. Physiol.* **2012**, *302*, H1219–H1230.
11. Pearce, E.L.; Pearce, E.J. Metabolic Pathways in Immune Cell Activation and Quiescence. *Immunity* **2013**, *38*, 633–643.
12. Cheng, S.C.; Quintin, J.; Cramer, R.A.; Shepardson, K.M.; Saeed, S.; Kumar, V.; Giamarellos-Bourboulis, E.J.; Martens, J.H.A.; Rao, N.A.; Aghajanirefah, A.; et al. MTOR- and HIF-1α-Mediated Aerobic Glycolysis as Metabolic Basis for Trained Immunity. *Science* **2014**, *345*, 1250684.
13. Needham, E.J.; Parker, B.L.; Burykin, T.; James, D.E.; Humphrey, S.J. Illuminating the Dark Phosphoproteome. *Sci. Signal.* **2019**, *12*, eaau8645.

14. Liu, S.; Zhu, L.; Xie, G.; Mok, B.W.Y.; Yang, Z.; Deng, S.; Lau, S.Y.; Chen, P.; Wang, P.; Chen, H.; et al. Potential Antiviral Target for SARS-CoV-2: A Key Early Responsive Kinase during Viral Entry. *CCS Chem.* **2022**, *4*, 112–121.

15. Xie, G.; Zhu, L.; Song, Y.; Huang, W.; Hu, D.; Cai, Z. An Integrated Quantitative Proteomics Strategy Reveals the Dual Mechanisms of Celastrol against Acute Inflammation. *Chin. Chem. Lett.* **2021**, *32*, 2164–2168.

16. Xie, G.; Zhu, L.; Liu, S.; Li, C.; Diao, X.; Zhang, Y.; Su, X.; Song, Y.; Cao, G.; Zhong, L.; et al. Multi-Omics Analysis of Attenuated Variant Reveals Potential Evaluation Marker of Host Damaging for SARS-CoV-2 Variants. *Sci. China Life Sci.* **2024**, *67*, 83–95.

17. Zhao, J.; Liu, H.; Chen, Q.; Xia, M.; Wan, L.; Yu, W.; Liu, C.; Hao, X.; Tang, C.; Chen, G.; et al. Mechanistic Study of Celastrol-Mediated Inhibition of Proinflammatory Activation of Macrophages in IgA Nephropathy via down-Regulating ECM1. *Int. J. Biol. Sci.* **2024**, *20*, 5731–5746.

18. Shirai, T.; Nakai, A.; Ando, E.; Fujimoto, J.; Leach, S.; Arimori, T.; Higo, D.; van Eerden, F.J.; Tulyeu, J.; Liu, Y.C.; et al. Celastrol Suppresses Humoral Immune Responses and Autoimmunity by Targeting the COMMD3/8 Complex. *Sci. Immunol.* **2023**, *8*, eadc9324.

19. Chang-Lun, H.; Der-Yuan, C.; Chih-Chen, T.; Jhen-Wei, L.; Bor-Show, T.; Tsai-Ching, H. Celastrol Attenuates Human Parvovirus B19 NS1-induced NLRP3 Inflammasome Activation in Macrophages. *Mol. Med. Rep.* **2023**, *28*, 193.

20. Venkatesha, S.H.; Dudics, S.; Astry, B.; Moudgil, K.D. Control of Autoimmune Inflammation by Celastrol, a Natural Triterpenoid. *Pathog. Dis.* **2016**, *74*, ftw059.

21. Wang, S.; Huang, Z.; Lei, Y.; Han, X.; Tian, D.; Gong, J.; Liu, M. Celastrol Alleviates Autoimmune Hepatitis Through the PI3K/AKT Signaling Pathway Based on Network Pharmacology and Experiments. *Front. Pharmacol.* **2022**, *13*, 816350.

22. Nakedi, K.C.; Calder, B.; Banerjee, M.; Giddey, A.; Nel, A.J.M.; Garnett, S.; Blackburn, J.M.; Soares, N.C. Identification of Novel Physiological Substrates of Mycobacterium Bovis BCG Protein Kinase G (PknG) by Label-Free Quantitative Phosphoproteomics. *Mol. Cell. Proteom.* **2018**, *17*, 1365.

23. Lien, E.C.; Lyssiotis, C.A.; Cantley, L.C. Metabolic Reprogramming by the PI3K-Akt-MTOR Pathway in Cancer. *Recent Results Cancer Res.* **2016**, *207*, 39–72.

24. Steelman, L.S.; Chappell, W.H.; Abrams, S.L.; Kempf, C.R.; Long, J.; Laidler, P.; Mijatovic, S.; Maksimovic-Ivanic, D.; Stivala, F.; Mazzarino, M.C.; et al. Roles of the Raf/MEK/ERK and PI3K/PTEN/Akt/MTOR Pathways in Controlling Growth and Sensitivity to Therapy-Implications for Cancer and Aging. *Aging* **2011**, *3*, 192.

25. Kuo, W.L.; Sharifi, M.N.; Lingen, M.W.; Ahmed, O.; Liu, J.; Nagilla, M.; Macleod, K.F.; Cohen, E.E.W. P62/SQSTM1 Accumulation in Squamous Cell Carcinoma of Head and Neck Predicts Sensitivity to Phosphatidylinositol 3-Kinase Pathway Inhibitors. *PLoS ONE* **2014**, *9*, e90171.

26. Wang, C.; Palavicini, J.P.; Wang, M.; Chen, L.; Yang, K.; Crawford, P.A.; Han, X. Comprehensive and Quantitative Analysis of Polyphosphoinositide Species by Shotgun Lipidomics Revealed Their Alterations in Db/Db Mouse Brain. *Anal. Chem.* **2016**, *88*, 12137–12144.

27. Arsham, A.M.; Plas, D.R.; Thompson, C.B.; Celeste Simon, M. Phosphatidylinositol 3-Kinase/Akt Signaling Is Neither Required for Hypoxic Stabilization of HIF-1 Alpha nor Sufficient for HIF-1-Dependent Target Gene Transcription. *J. Biol. Chem.* **2002**, *277*, 15162–15170.

28. Taylor, C.T.; Scholz, C.C. The Effect of HIF on Metabolism and Immunity. *Nat. Rev. Nephrol.* **2022**, *18*, 573–587.

29. Mylonis, I.; Chachami, G.; Samiotaki, M.; Panayotou, G.; Paraskeva, E.; Kalousi, A.; Georgatsou, E.; Bonanou, S.; Simos, G. Identification of MAPK Phosphorylation Sites and Their Role in the Localization and Activity of Hypoxia-Inducible Factor-1alpha. *J. Biol. Chem.* **2006**, *281*, 33095–33106.

30. Tannahill, G.M.; Curtis, A.M.; Adamik, J.; Palsson-Mcdermott, E.M.; McGettrick, A.F.; Goel, G.; Frezza, C.; Bernard, N.J.; Kelly, B.; Foley, N.H.; et al. Succinate Is a Danger Signal That Induces IL-1β via HIF-1α. *Nature* **2013**, *496*, 238.

31. Lian, G.; Li, X.; Zhang, L.; Zhang, Y.; Sun, L.; Zhang, X.; Liu, H.; Pang, Y.; Kong, W.; Zhang, T.; et al. Macrophage Metabolic Reprogramming Aggravates Aortic Dissection through the HIF1α-ADAM17 Pathway☆. *EBioMedicine* **2019**, *49*, 291–304.

32. Dang, B.; Gao, Q.; Zhang, L.; Zhang, J.; Cai, H.; Zhu, Y.; Zhong, Q.; Liu, J.; Niu, Y.; Mao, K.; et al. The Glycolysis/HIF-1α Axis Defines the Inflammatory Role of IL-4-Primed Macrophages. *Cell Rep.* **2023**, *42*, 112471.

33. Jha, A.K.; Huang, S.C.C.; Sergushichev, A.; Lampropoulou, V.; Ivanova, Y.; Loginicheva, E.; Chmielewski, K.; Stewart, K.M.; Ashall, J.; Everts, B.; et al. Network Integration of Parallel Metabolic and Transcriptional Data Reveals Metabolic Modules That Regulate Macrophage Polarization. *Immunity* **2015**, *42*, 419–430.

34. Metallo, C.M.; Gameiro, P.A.; Bell, E.L.; Mattaini, K.R.; Yang, J.; Hiller, K.; Jewell, C.M.; Johnson, Z.R.; Irvine, D.J.; Guarente, L.; et al. Reductive Glutamine Metabolism by IDH1 Mediates Lipogenesis under Hypoxia. *Nature* **2011**, *481*, 380–384.

35. Lee, J.H.; Koo, T.H.; Yoon, H.; Jung, H.S.; Jin, H.Z.; Lee, K.; Hong, Y.S.; Lee, J.J. Inhibition of NF-KB Activation through Targeting IκB Kinase by Celastrol, a Quinone Methide Triterpenoid. *Biochem. Pharmacol.* **2006**, *72*, 1311–1321.

36. Zhao, J.; Sun, Y.; Shi, P.; Dong, J.N.; Zuo, L.G.; Wang, H.G.; Gong, J.F.; Li, Y.; Gu, L.L.; Li, N.; et al. Celastrol Ameliorates Experimental Colitis in IL-10 Deficient Mice via the up-Regulation of Autophagy. *Int. Immunopharmacol.* **2015**, *26*, 221–228.

37. Ersahin, T.; Tuncbag, N.; Cetin-Atalay, R. The PI3K/AKT/MTOR Interactive Pathway. *Mol. Biosyst.* **2015**, *11*, 1946–1954.

38. Li, W.; Tang, X.; Zheng, Y.; Xu, X.; Zhao, N.; Tsao, B.P.; Feng, X.; Sun, L. Phosphatidic Acid Promoting the Generation of Interleukin-17A Producing Double-Negative T Cells by Enhancing MTORC1 Signaling in Lupus. *Arthritis Rheumatol.* **2024**, *76*, 1096–1108.

39. Jiang, S.; Yang, H.; Li, M. Emerging Roles of Lysophosphatidic Acid in Macrophages and Inflammatory Diseases. *Int. J. Mol. Sci.* **2023**, *24*, 12524.

40. Choy, C.H.; Han, B.K.; Botelho, R.J. Phosphoinositide Diversity, Distribution, and Effector Function: Stepping Out of the Box. *Bioessays* **2017**, *39*, 12524.

41. Shulga, Y.V.; Anderson, R.A.; Topham, M.K.; Epand, R.M. Phosphatidylinositol-4-Phosphate 5-Kinase Isoforms Exhibit Acyl Chain Selectivity for Both Substrate and Lipid Activator. *J. Biol. Chem.* **2012**, *287*, 35953–35963.

42. Schmid, A.C.; Wise, H.M.; Mitchell, C.A.; Nussbaum, R.; Woscholski, R. Type II Phosphoinositide 5-Phosphatases Have Unique Sensitivities towards Fatty Acid Composition and Head Group Phosphorylation. *FEBS Lett.* **2004**, *576*, 9–13.

43. Barneda, D.; Janardan, V.; Niewczas, I.; Collins, D.M.; Cosulich, S.; Clark, J.; Stephens, L.R.; Hawkins, P.T. Acyl Chain Selection Couples the Consumption and Synthesis of Phosphoinositides. *EMBO J.* **2022**, *41*, e110038.

44. Kim, Y.J.; Sengupta, N.; Sohn, M.; Mandal, A.; Pemberton, J.G.; Choi, U.; Balla, T. Metabolic Routing Maintains the Unique Fatty Acid Composition of Phosphoinositides. *EMBO Rep.* **2022**, *23*, e54532.

45. Michell, R.H. Inositol Phospholipids and Cell Surface Receptor Function. *BBA—Rev. Biomembr.* **1975**, *415*, 81–147.

46. Manni, M.M.; Tiberti, M.L.; Pagnotta, S.; Barelli, H.; Gautier, R.; Antonny, B. Acyl Chain Asymmetry and Polyunsaturation of Brain Phospholipids Facilitate Membrane Vesiculation without Leakage. *Elife* **2018**, *7*, e34394.

47. Albanese, A.; Daly, L.A.; Mennerich, D.; Kietzmann, T.; Sée, V. The Role of Hypoxia-Inducible Factor Post-Translational Modifications in Regulating Its Localisation, Stability, and Activity. *Int. J. Mol. Sci.* **2020**, *22*, 268.

48. Zhou, J.; Fandrey, J.; Schümann, J.; Tiegs, G.; Brüne, B. NO and TNF-Alpha Released from Activated Macrophages Stabilize HIF-1alpha in Resting Tubular LLC-PK1 Cells. *Am. J. Physiol. Cell Physiol.* **2003**, *284*, C439–C46

49. Corcoran, S.E.; O'Neill, L.A.J. HIF1α and Metabolic Reprogramming in Inflammation. *J. Clin. Investig.* **2016**, *126*, 3699–3707.

50. Huang, L.; Zhang, Z.; Zhang, S.; Ren, J.; Zhang, R.; Zeng, H.; Li, Q.; Wu, G. Inhibitory Action of Celastrol on Hypoxia-Mediated Angiogenesis and Metastasis via the HIF-1α Pathway. *Int. J. Mol. Med.* **2011**, *27*, 407–415.

51. Palmieri, E.M.; Gonzalez-Cotto, M.; Baseler, W.A.; Davies, L.C.; Ghesquière, B.; Maio, N.; Rice, C.M.; Rouault, T.A.; Cassel, T.; Higashi, R.M.; et al. Nitric Oxide Orchestrates Metabolic Rewiring in M1 Macrophages by Targeting Aconitase 2 and Pyruvate Dehydrogenase. *Nat. Commun.* **2020**, *11*, 698

52. Li, Y.; Li, Y.C.; Liu, X.T.; Zhang, L.; Chen, Y.H.; Zhao, Q.; Gao, W.; Liu, B.; Yang, H.; Li, P. Blockage of Citrate Export Prevents TCA Cycle Fragmentation via Irg1 Inactivation. *Cell Rep.* **2022**, *38*, 110391.

53. Joo, H.Y.; Jung, J.K.; Kim, M.Y.; Woo, S.R.; Jeong, J.M.; Park, E.R.; Kim, Y.M.; Park, J.J.; Kim, J.; Yun, M.; et al. NADH Elevation during Chronic Hypoxia Leads to VHL-Mediated HIF-1α Degradation via SIRT1 Inhibition. *Cell Biosci.* **2023**, *13*, 182.

54. Cramer, T.; Yamanishi, Y.; Clausen, B.E.; Förster, I.; Pawlinski, R.; Mackman, N.; Haase, V.H.; Jaenisch, R.; Corr, M.; Nizet, V.; et al. HIF-1α Is Essential for Myeloid Cell-Mediated Inflammation. *Cell* **2003**, *112*, 645–657.

55. Kelly, B.; O'Neill, L.A.J. Metabolic Reprogramming in Macrophages and Dendritic Cells in Innate Immunity. *Cell Res.* **2015**, *25*, 771–784.

56. Li, W.; Cai, Z.N.; Mehmood, S.; Liang, L.L.; Liu, Y.; Zhang, H.Y.; Chen, Y.; Lu, Y.M. Anti-Inflammatory Effects of Morchella Esculenta Polysaccharide and Its Derivatives in Fine Particulate Matter-Treated NR8383 Cells. *Int. J. Biol. Macromol.* **2019**, *129*, 904–915.

57. Wong, L.Y.F.; Cheung, B.M.Y.; Li, Y.Y.; Tang, F. Adrenomedullin Is Both Proinflammatory and Antiinflammatory: Its Effects on Gene Expression and Secretion of Cytokines and Macrophage Migration Inhibitory Factor in NR8383 Macrophage Cell Line. *Endocrinology* **2005**, *146*, 1321–1327.

58. Chen, S.; Hu, Y.; Zhang, J.; Zhang, P. Anti-inflammatory Effect of Salusin-β Knockdown on LPS-activated Alveolar Macrophages via NF-κB Inhibition and HO-1 Activation. *Mol. Med. Rep.* **2021**, *23*, 127.